Supporting Information

Constructing weak Ru–Mo metallic bonds to suppress Ru overoxidation for

durable acidic water oxidation

Yongduo Liu,[a] Runxu Deng,[a] Yang Song,[a] Weiling Tan,[a] Xiongxin Tao,[a] Shijian Luo,[a] Daojun Long,*[a] Siguo Chen*[a] and Zidong Wei [a]

[a]State Key Laboratory of Advanced Chemical Power Sources (SKL-ACPS), College of Chemistry and Chemical Engineering, Chongqing University, Chongqing 401331, P. R. China

*Email: csg810519@126.com

Experimental section

Preparation of D301 powder. Firstly, 250 mL of deionized water (DI), 1 M HCl solution, 1 M NaCl solution, or 1 M NaOH solution was injected four times into an ion exchange column containing 50 g of D301 pellets to remove inorganic and organic substances in the D301 pellets. A large volume of DI was then used to further remove impurities from the D301 pellets. The cleaned D301 pellets were transferred to a desiccator, heated to 40 °C and held at this temperature for approximately 24 hours. These D301 pellets were finally pulverized to powder by grinding at 3000 rpm in a high-speed rotor mill.

Synthesis of K_2RuCl_6. Typically, 5.00 g $RuCl_3 \cdot xH_2O$ and 2.73 g KCl were dissolved in 200 mL DI. Under magnetic stirring, 40 mL of ethanol and 5 mL of concentrated hydrochloric acid were added. Subsequently, the solution was transferred to a magnetic oil bath and condensed under reflux at 110°C for 3 hours. When the solution turns reddish brown, it can be dried to obtain K_2RuCl_6.

Synthesis of $Mo_xRu_{1-x}O_2$ (x = 0, 0.125, 0.25, 0.5) catalysts. Typically, 343.0 mg K_2RuCl_6 (0.875 mmol) and 24.5 mg $(NH_4)_2MoO_4$ (0.125 mmol) were dissolved in 30 mL of DI to form a precursor solution. Then, 3.00 g of powdered D301 anion exchange resin was added to the solution, followed by magnetic stirring at room temperature for 8 hours. After sufficient ion exchange, the suspension was vacuum filtered and then dried at 80°C for 8 hours. The resulting powder containing Ru and Mo was then calcined in air under ambient pressure at 450 °C for 8 hours. After cooling the furnace to room temperature, the black products were collected. The obtained products were washed several times with 40 mL of DI and then dried in a vacuum oven at 60°C to finally obtain the $Mo_{0.125}Ru_{0.875}O_2$ sample. To synthesize the $Mo_0Ru_1O_2$, $Mo_{0.25}Ru_{0.75}O_2$ and $Mo_{0.5}Ru_{0.5}O_2$ samples, the same procedure was used with the $Mo_{0.125}Ru_{0.875}O_2$ sample by changing the amount of K_2RuCl_6 (392.0 mg, 294.0 mg, 196.0 mg) and $(NH_4)_2MoO_4$ (0 mg, 49.0 mg, and 98.0 mg).

Structure and composition of the catalysts. Powder X-ray diffractometer (XRD) was performed on a Panalytical X'pert with Cu Kα radiation (λ = 1.542 Å) at room temperature to obtain the crystalline structure of the samples. The X-ray photoelectron spectroscopy (XPS) signals of the samples were collected with an ESCALAB250Xi spectrometer with an Al Kα light source (Al Kα, 1.4866 keV). For transmission electron microscopy (TEM), a FEI Talos F200S instrument was used to characterize the microstructure of the samples under an accelerating voltage of 200 kV, and corresponding energy dispersive X-ray (EDS) mapping was employed to identify the element composition and distribution. Electron paramagnetic resonance (EPR) spectra were obtained on a Bruker EMXPLUS spectrometer with a microwave frequency of 9.84 GHz. The X-ray absorption spectroscopy (XAFS) study was performed at the BL14B2 of SPring-8 (8 GeV, 100 mA), Japan, in which, the X-ray beam was mono-chromatized with water-cooled Si (311) double-crystal monochromator and focused with two Rh coated focusing mirrors with the beam size of 2.0 mm in the horizontal direction and 0.5 mm in the vertical direction around sample position, to obtain X-ray adsorption fine structure (XAFS) spectra both in near and extended edge.

Electrochemical measurements. A conventional three-electrode system in Gamry electrochemical workstation (Reference 3000) was employed to evaluate the electrochemical performance of the samples. Ag/AgCl (3.5 M KCl-saturated) and graphite rods (Φ = 6 mm) served as the reference electrode (RE) and counter electrode (CE), respectively. The catalyst ink was prepared by dispersing 4 mg of catalyst into a mixture of 1 mL ethanol and 15 μL Nafion solution (5 wt%), followed by ultrasonic dispersion. Then, 15 μL of the abovementioned ink was dropped onto a cleaned glassy carbon (GC) electrode (Φ = 5 mm) and dried under an infrared lamp to form the working electrode (WE) with the catalysts. In all experiments, the electrolyte was 0.1 M perchloric acid ($HClO_4$) solution. Before testing, the Ag/AgCl electrode was calibrated by cyclic voltammetry (CV) using a purified Pt mesh as the WE in H_2-saturated 0.1 M $HClO_4$ electrolyte, and the average voltage value was recorded as E_c when the current was zero. The value of E_c was generally between 0.260 V and 0.270 V for the Ag/AgCl electrode in 0.1 M $HClO_4$ solution. All potentials were calibrated relative to the reversible hydrogen electrode (RHE) with iR compensation, according to the following calculations:

$$E_{RHE} = E_{Ag/AgCl} + E_c - I_{mea} \times R_s$$

where $E_{Ag/AgCl}$ is the potential relative to the Ag/AgCl electrode, which is the set potential during all measurements, and E_c is the potential of the Ag/AgCl electrode relative to the RHE. I_{mea} is the measured

polarization current. R_s is the solution resistance.

To assess the true OER performance, the WEs were first subjected to 50 cycles of CV between 1.0 and 1.5 V (vs. RHE) at a scan rate of 50 mV s^{-1} to stabilize the catalysts in an O$_2$-saturated 0.1 M HClO$_4$ solution. Then, linear sweep voltammetry (LSV) was used to measure the OER polarization curve from 1.0 to 1.6 V (vs. RHE) at a sweep rate of 5 mV s^{-1} with a 1600 rpm rotation speed. Electrochemical impedance spectroscopy (EIS) was obtained in the frequency range from 10^5 Hz to 10^{-2} Hz at a bias voltage of 1.4 V (vs. RHE) with a 10 mV of amplitude. To investigate the stability of the catalysts, carbon paper (CP, with a surface area of 1 cm^2) with 2.0 mg of catalyst was employed as the WEs, and then chronopotentiometry was used to record the E-t curve at a current density of 10 mA cm^{-2}.

The ECSA were calculated in the revised version via the following equation:

$$ECSA = C_{dl}/C_s$$

where ECSA is the electrochemical active surface area (cm^2), C$_{dl}$ is double layer capacitance (mF), and C$_s$ is the specific capacitance (C$_s$ = 0.035 mF cm^{-2}).

Electrochemical measurement of PEMWE. During the process of constructing the membrane electrode assembly (MEA), Mo$_{0.125}$Ru$_{0.875}$O$_2$ are used as anode catalysts, while commercial Pt/C (40 wt%, Johnson Matthey) is employed as the cathode catalyst. To prepare the anode and cathode inks, the catalysts are dispersed in a mixture of isopropanol and deionized water in a ratio of 2:3. Subsequently, a 5 wt% Nafion solution is added to achieve an ionomer content of 38 wt% for the anode and 40 wt% for the cathode. After ultrasonic treatment in a low-temperature water bath for at least one hour, a uniform catalyst ink can be obtained. To fabricate the MEA with Nafion 115 membrane as the electrolyte, the anode and cathode catalysts are directly sprayed onto both sides of the Nafion 115 membrane using an ultrasonic spraying system. After optimizing the catalyst loading, it is controlled at 2 mg$_{Ru}$ cm^{-2} and 0.3 mg$_{Pt}$ cm^{-2}, respectively. After cooling and peeling, a catalyst-coated membrane (CCM) is obtained and stored in deionized water for further measurements. To construct a proton exchange membrane electrolyzer for performance evaluation, a titanium felt with a thickness of 500 μm is used as the porous transport layer (PTL) for both the anode and cathode. The assembly pressure of the fixture is set at 6 N m, and the active area of the electrodes is measured at 9 cm^2. The proton exchange membrane electrolyzer operates at 80°C, using deionized water as the reactant, with a flow rate of 40 mL min^{-1}. Polarization curves are collected in the range of 0.1 to 3.5 A cm^{-2}.

Differential electrochemical mass spectrometry (DEMS) analysis. In situ DEMS involving heavy-oxygen water (H$_2$^{18}O) was performed to identify the level of participation for lattice oxygen during the OER process in a QAS 100 device. The catalysts were dripped onto a porous gold (Au) disk electrode with a catalyst loading of 0.1 mg cm^{-2}. The porous Au disk electrode with catalysts, Ag/AgCl electrode and pure Pt wire were used as the WE, RE and CE, respectively. First, the catalysts were labeled with ^{18}O isotope by 4 CV cycles at a scan rate of 5 mV s^{-1} in 0.1 M HClO$_4$ solution containing H$_2$^{18}O. Considering the difference in activity between Mo$_{0.125}$Ru$_{0.875}$O$_2$ and Com-RuO$_2$, the potential range of CV cycles was set as 0.9-1.25 V (vs. Ag/AgCl) for Mo$_{0.125}$Ru$_{0.875}$O$_2$ and 0.9-1.6 V (vs. Ag/AgCl) for Com-RuO$_2$ to achieve a similar current intensity. Then, the resulting electrodes were rinsed with ^{16}O water several times to remove the residual H$_2$^{18}O. Finally, the electrodes were placed in 0.1 M HClO$_4$ containing H$_2$^{16}O, and CV was carried out within the above potential windows. Meanwhile, mass spectrometry was used to detect O$_2$ generated during the OER process in real time.

Details of the computational studies. Density functional theory (DFT) calculations were conducted via the Vienna Ab initio Simulation Package (VASP). The electronic structures of materials were described by the generalized gradient approximation (GGA) of Perdew-Burke-Ernzerhof (PBE) and the projector augmented wave (PAW)[1-3]. The kinetic cutoff energy of the plane wave was fixed at 450 eV. The convergence tolerance of force and energy for each atom were 0.02 eV/Å and 10^{-5} eV, respectively[4, 5].

A unit cell of pristine RuO$_2$ contained 48 atoms, including 16 Ru atoms and 32 O atoms. On this basis, we constructed the doped model according to the Mo proportion from ICP-AES (Table S1). During the structural optimization process, Brillouin zone integration was performed with 3 × 3 × 4 gamma k-point sampling. All
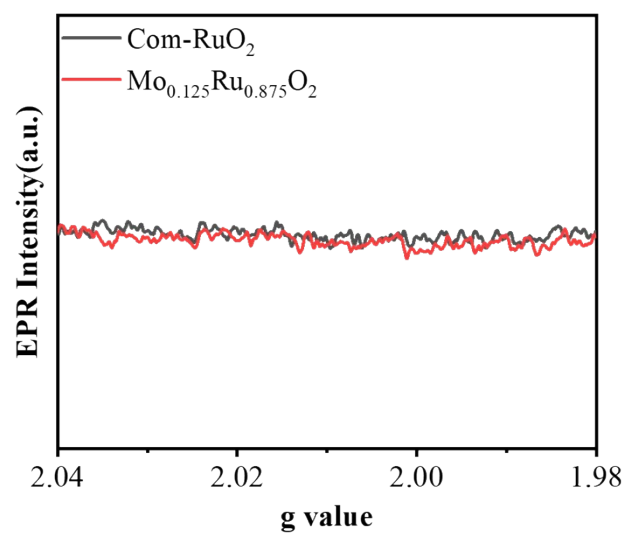
atoms and lattice parameters were free to vary. According to the principle of energy minimization, the most stable structure was selected to perform subsequent calculations. Detailed information on the model structures after optimization is provided in Fig. S2-5.

For the slab model, pristine RuO_2 had a four-layer Ru-O structure, contained 64 Ru atoms and 128 O atoms. The Mo-doped RuO_2 slab had the same specifications. However, XPS showed that Mo was enriched on the surface of Mo-doped RuO_2(Fig. S14). Therefore, the slab models of Mo-doped RuO_2 were reassigned based on the actual concentration on the catalyst surface (Table. S4). Furthermore, both XPS (Fig. S13) and DFT results (Fig. S16) indicate that the Mo sites on the reaction interface not only have a strong tendency towards hydroxylation, but also act only as electron modulators and do not participate in the OER process. This suggests that the Mo sites on the real reaction interface are saturated with oxygen intermediates, thus constructing the oxygen-saturated slab model. Furthermore, the top two layers were relaxed, and the bottom two layers were set to be static to simulate the surface relaxation. Monkhorst-Pack k-point sampling ($2 \times 2 \times 1$ and $4 \times 4 \times 1$) was applied for geometric optimization and density of states (DOS) calculations, respectively. Detailed information on the model structures after optimization is provided in Fig. S15.
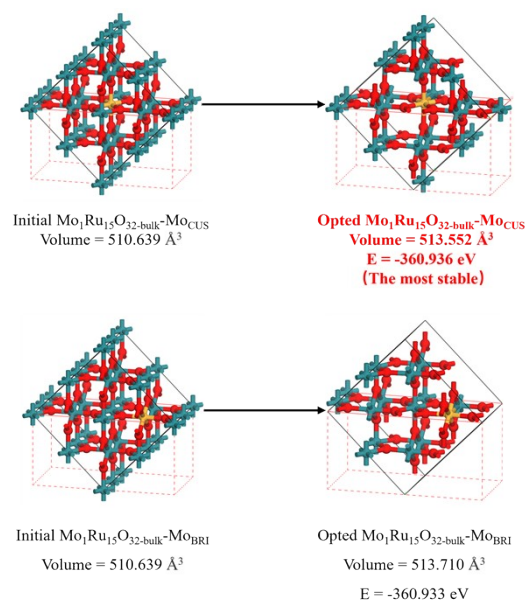
To evaluate catalyst activity, models of the reaction intermediates (OH^*, O^* and OOH^*) adsorbed on the RuO_2 and Mo-doped RuO_2 catalysts were also constructed, and each model was optimized to the most stable state. The free energy (ΔG) of each OER step was calculated according to the following equation[6, 7]:

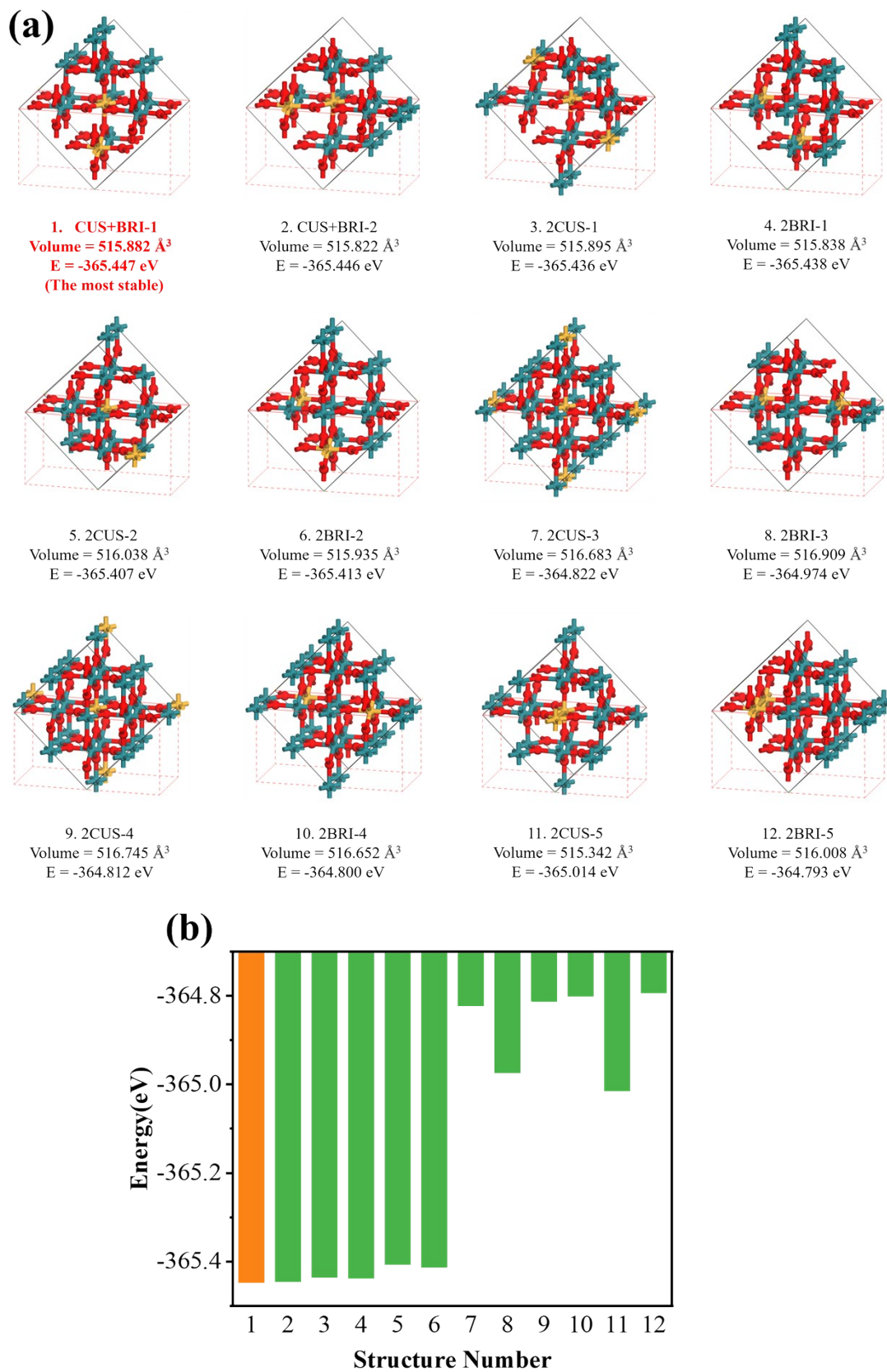$$\Delta G = \Delta E + \Delta E_{ZPE} - T \times \Delta S$$

where ΔE is the energy difference between before and after the reaction; ΔE_{ZPE} is the zero-point energy difference at 298.15 K; T is the experimental temperature (298.15 K); and ΔS is the entropy change.
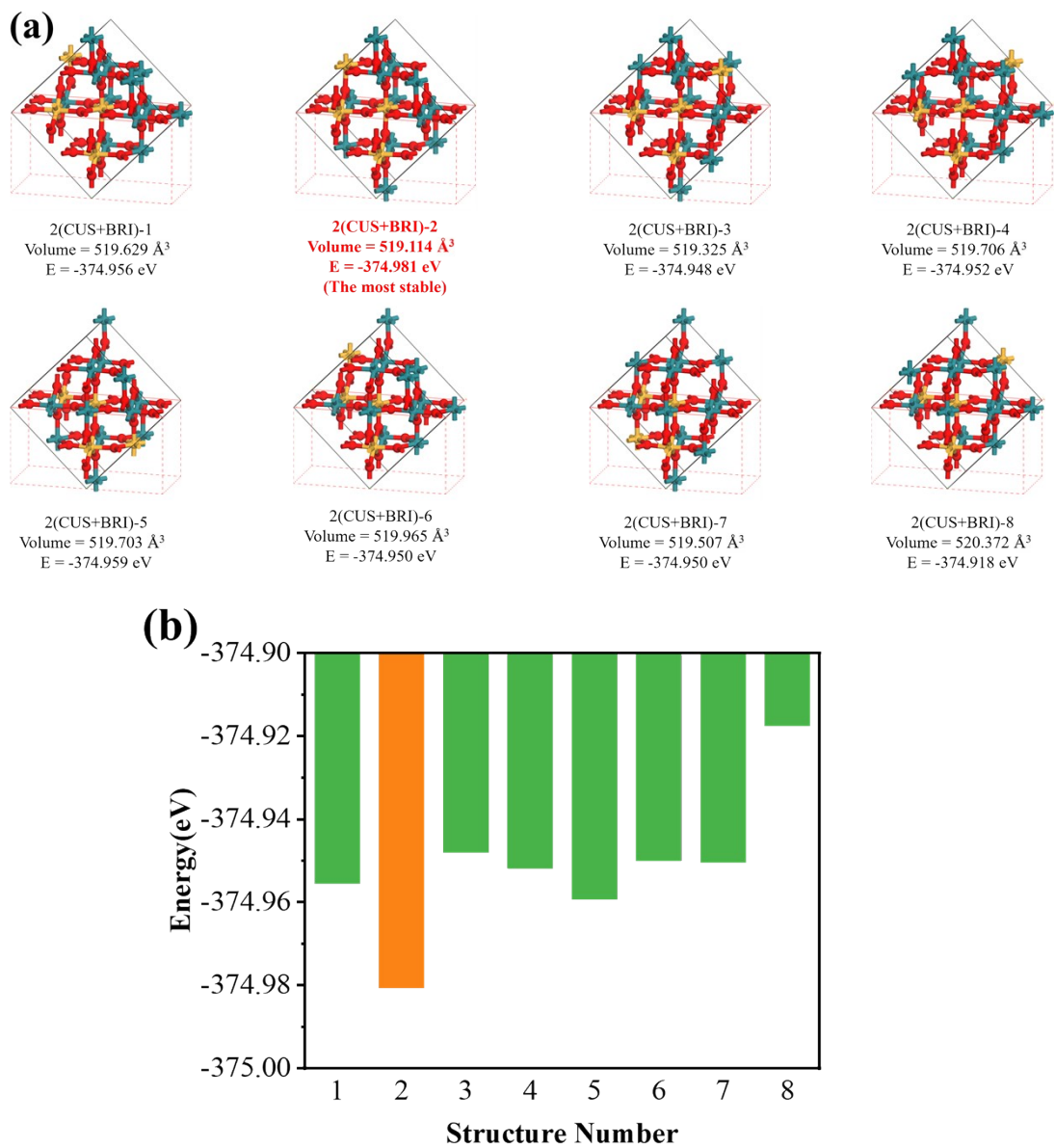
Fig. S1 EPR spectra of Com-RuO$_2$ and Mo$_{0.125}$Ru$_{0.875}$O$_2$.

Initial Mo$_1$Ru$_{15}$O$_{32\text{-bulk}}$-Mo$_{CUS}$
Volume = 510.639 Å^3

Opted Mo$_1$Ru$_{15}$O$_{32\text{-bulk}}$-Mo$_{CUS}$
Volume = 513.552 Å^3
E = -360.936 eV
（The most stable）

Initial Mo$_1$Ru$_{15}$O$_{32\text{-bulk}}$-Mo$_{BRI}$
Volume = 510.639 Å^3

Opted Mo$_1$Ru$_{15}$O$_{32\text{-bulk}}$-Mo$_{BRI}$
Volume = 513.710 Å^3
E = -360.933 eV

Fig. S2 Structures, volume and energy of Mo$_1$Ru$_{15}$O$_{32\text{-bulk}}$ with Mo$_{CUS}$ or Mo$_{BRI}$, where the green, orange and red sphere represents Ru, Mo and O atoms, respectively.

(a)

1. **CUS+BRI-1**
   Volume = 515.882 Å³
   E = -365.447 eV
   (The most stable)

2. CUS+BRI-2
   Volume = 515.822 Å³
   E = -365.446 eV

3. 2CUS-1
   Volume = 515.895 Å³
   E = -365.436 eV

4. 2BRI-1
   Volume = 515.838 Å³
   E = -365.438 eV

5. 2CUS-2
   Volume = 516.038 Å³
   E = -365.407 eV

6. 2BRI-2
   Volume = 515.935 Å³
   E = -365.413 eV

7. 2CUS-3
   Volume = 516.683 Å³
   E = -364.822 eV

8. 2BRI-3
   Volume = 516.909 Å³
   E = -364.974 eV

9. 2CUS-4
   Volume = 516.745 Å³
   E = -364.812 eV

10. 2BRI-4
    Volume = 516.652 Å³
    E = -364.800 eV

11. 2CUS-5
    Volume = 515.342 Å³
    E = -365.014 eV

12. 2BRI-5
    Volume = 516.008 Å³
    E = -364.793 eV

(b)

Fig. S3 a) Structures, volume and energy of $Mo_2Ru_{14}O_{32-bulk}$ established on the basis of the most stable $Mo_1Ru_{15}O_{32-bulk}$. **b)** Energy of all $Mo_2Ru_{14}O_{32-bulk}$ structures.

(a)

2(CUS+BRI)-1
Volume = 519.629 Å³
E = -374.956 eV

2(CUS+BRI)-2
Volume = 519.114 Å³
E = -374.981 eV
(The most stable)

2(CUS+BRI)-3
Volume = 519.325 Å³
E = -374.948 eV

2(CUS+BRI)-4
Volume = 519.706 Å³
E = -374.952 eV

2(CUS+BRI)-5
Volume = 519.703 Å³
E = -374.959 eV

2(CUS+BRI)-6
Volume = 519.965 Å³
E = -374.950 eV

2(CUS+BRI)-7
Volume = 519.507 Å³
E = -374.950 eV

2(CUS+BRI)-8
Volume = 520.372 Å³
E = -374.918 eV

(b)

Fig. S4 a) Structures, volume and energy of $Mo_4Ru_{12}O_{32-bulk}$ established on the basis of the most stable $Mo_2Ru_{14}O_{32-bulk}$. **b)** Energy of all $Mo_4Ru_{12}O_{32-bulk}$ structures.

(a)

4(CUS+BRI)-1
Volume = 524.700 Å³
E = -393.719 eV
(The most stable)

4(CUS+BRI)-2
Volume = 525.881 0 Å³
E = -393.670 eV

4(CUS+BRI)-3
Volume = 523.737 0 Å³
E = -389.151 eV

4(CUS+BRI)-4
Volume = 524.236 0 Å³
E = -388.942 eV

(b)
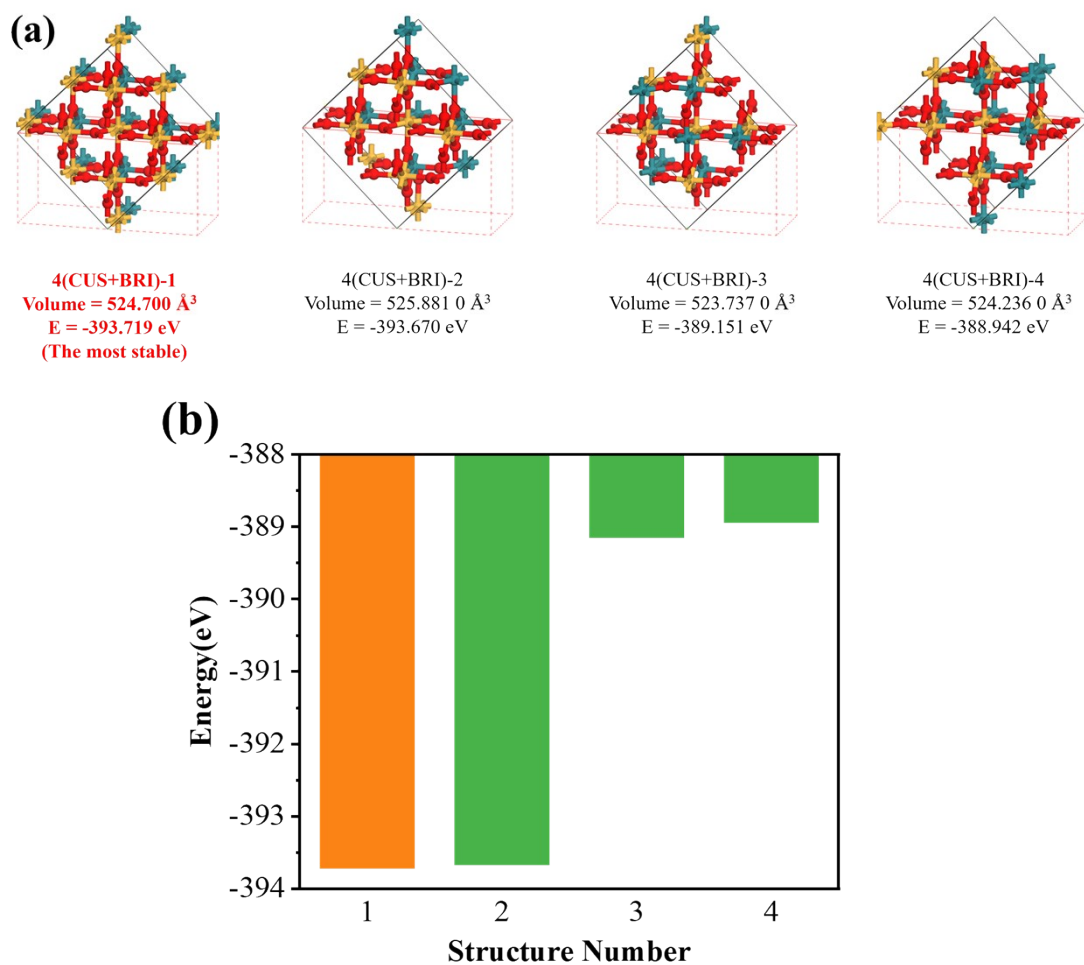
Fig. S5 a) Structures, volume and energy of $Mo_8Ru_8O_{32\text{-bulk}}$ established on the basis of the most stable $Mo_4Ru_{12}O_{32\text{-bulk}}$. **b)** Energy of all $Mo_8Ru_8O_{32\text{-bulk}}$ structures.
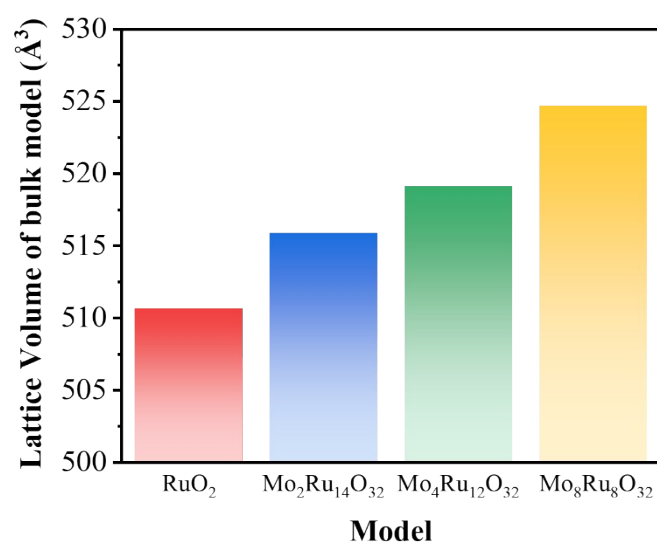
Fig. S6 Volumes of the bulk models with different Mo proportions according to DFT calculations.
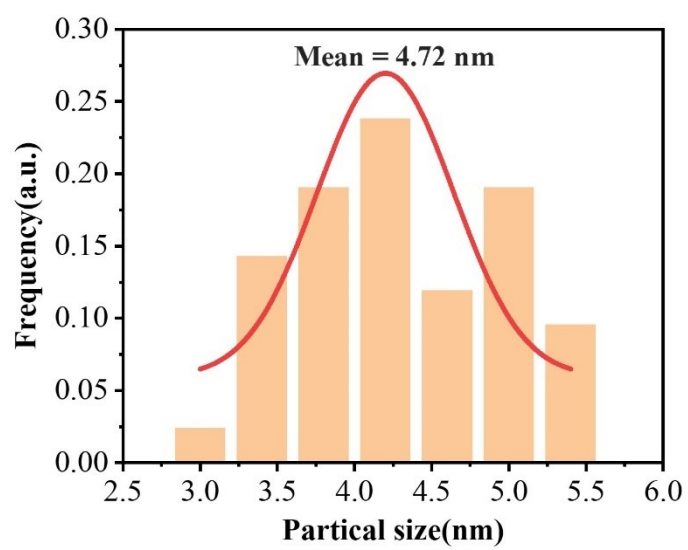
Fig. S7 Particle size distribution of $Mo_{0.125}Ru_{0.875}O_2$.

Ru$_{bulk}$ (P6$_3$/mmc)
Ru-Ru = 2.654/2.729 Å

RuO$_{2\text{-bulk}}$ (P4$_2$/mnm)
Ru-Ru = 3.124 Å

Mo$_2$Ru$_{14}$O$_{32\text{-bulk}}$
Ru-Mo = 2.891/3.260 Å

Mo$_4$Ru$_{12}$O$_{32\text{-bulk}}$
Ru-Mo = 2.729/3.207 Å

Mo$_8$Ru$_8$O$_{32\text{-bulk}}$
Ru-Mo = 2.668/3.079 Å
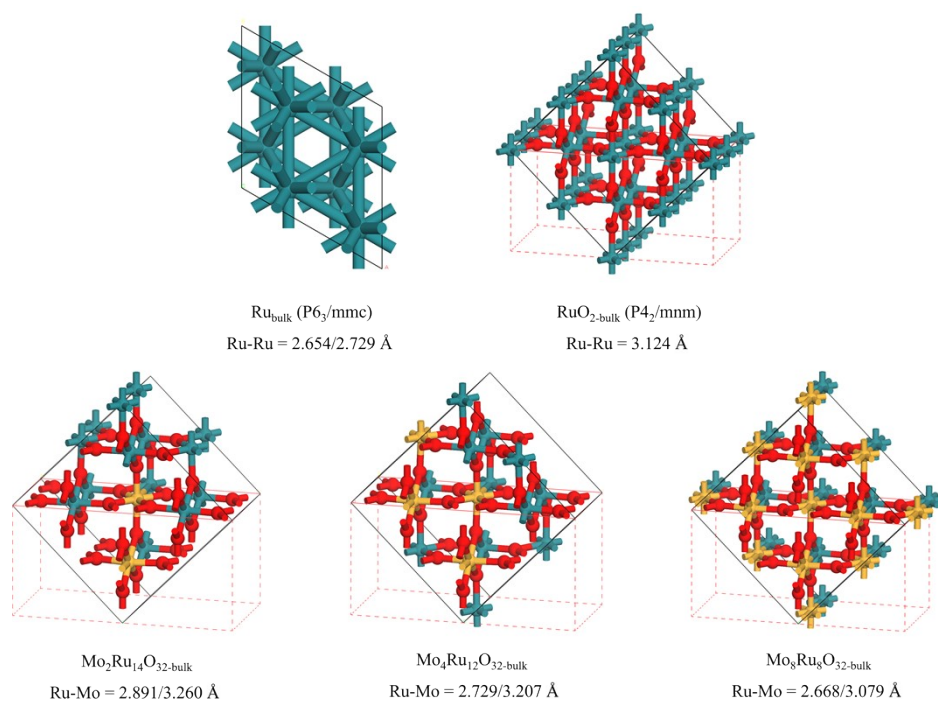
Fig. S8 Thermodynamically stable bulk structures and intermetallic coordination distances of Ru, RuO$_2$, and Mo-doped RuO$_2$.
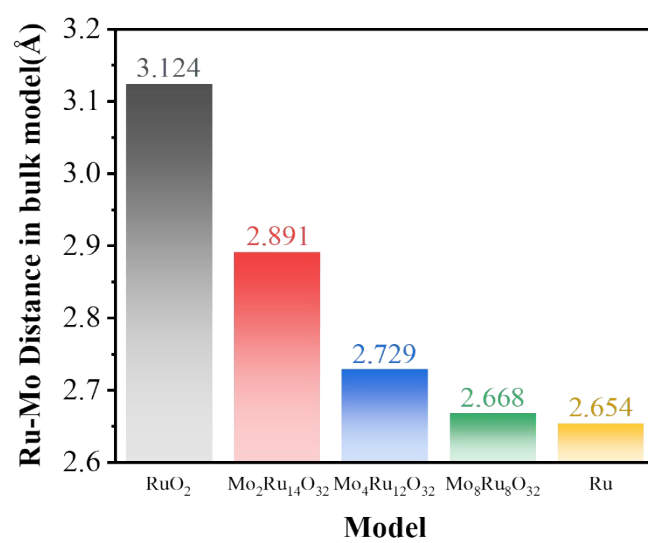
Fig. S9 Ru–M coordination distances in the bulk models with different Mo proportions.
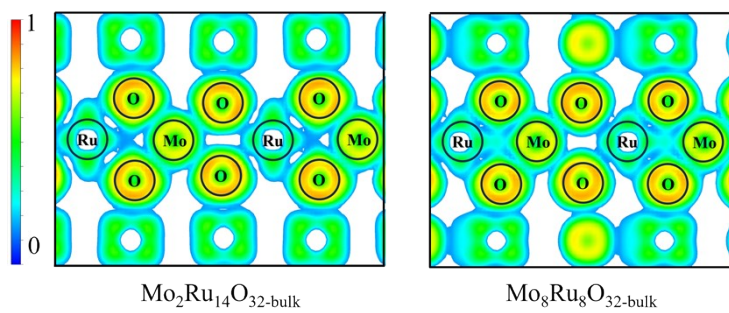
Fig. S10 ELF of $Mo_2Ru_{14}O_{32-bulk}$ and $Mo_8Ru_8O_{32-bulk}$, where the regions with intensities below 0.15 are removed.
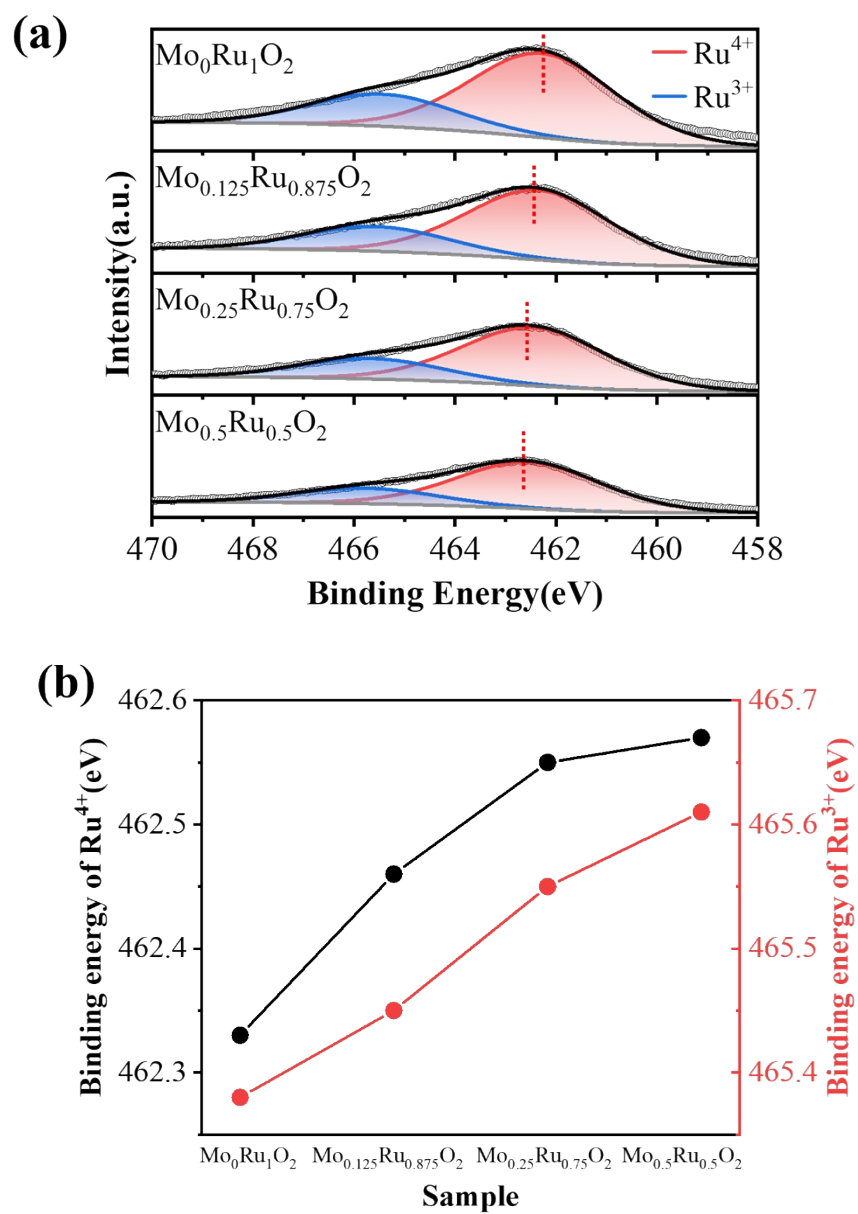
Fig. S11 a) Ru-3p XPS spectra of $Mo_xRu_{1-x}O_2$. b) Binding energies of Ru species in $Mo_xRu_{1-x}O_2$.

(b)

Mo$_{0.125}$Ru$_{0.875}$O$_2$

Mo$_{0.25}$Ru$_{0.75}$O$_2$

Mo$_{0.5}$Ru$_{0.5}$O$_2$

Intensity(a.u.)

— Mo^{5+}
— Mo^{6+}

238 236 234 232 230 228

Binding Energy(eV)

(b)

Binding energy of Mo^{5+}(eV)

Binding energy of Mo^{6+}(eV)

231.0
230.9
230.8
230.7

232.2
232.1
232.0
231.9

Mo$_{0.125}$Ru$_{0.875}$O$_2$ Mo$_{0.25}$Ru$_{0.75}$O$_2$ Mo$_{0.5}$Ru$_{0.5}$O$_2$

Sample
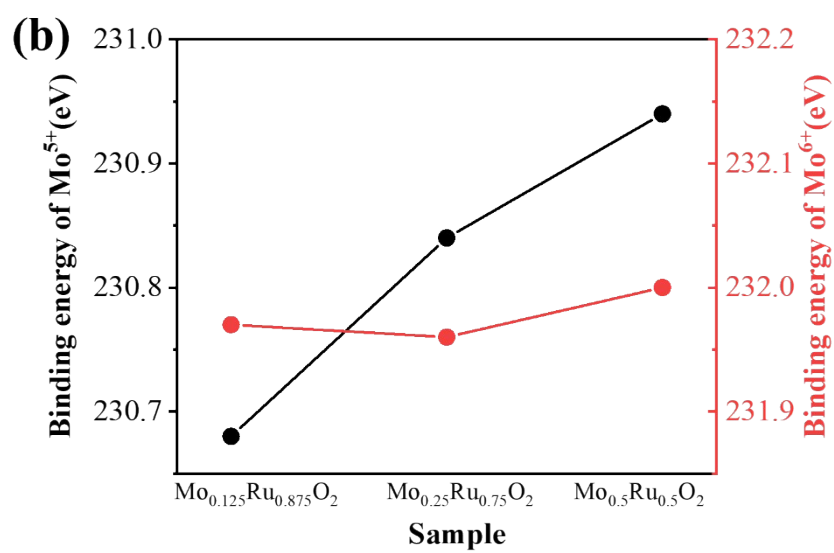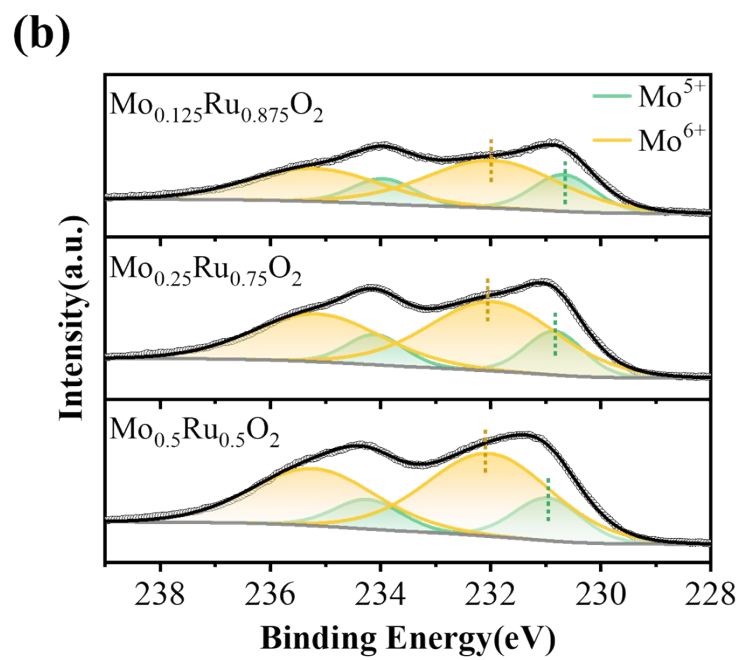
Fig. S12 a) Mo-3d XPS spectra of Mo$_x$Ru$_{1-x}$O$_2$. b) Binding energies of Mo species in Mo$_x$Ru$_{1-x}$O$_2$.
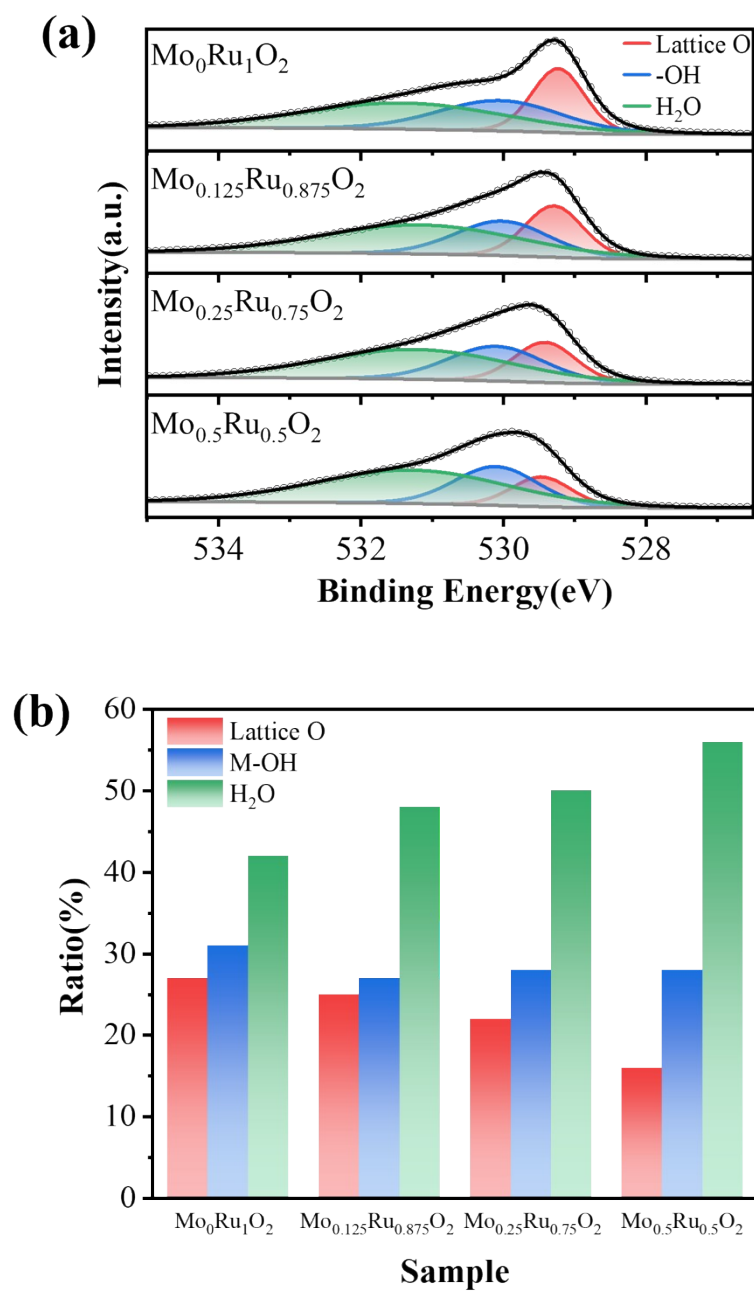
Fig. S13 a) O-1s XPS spectra of $Mo_xRu_{1-x}O_2$. b) Ratio of O species in $Mo_xRu_{1-x}O_2$.
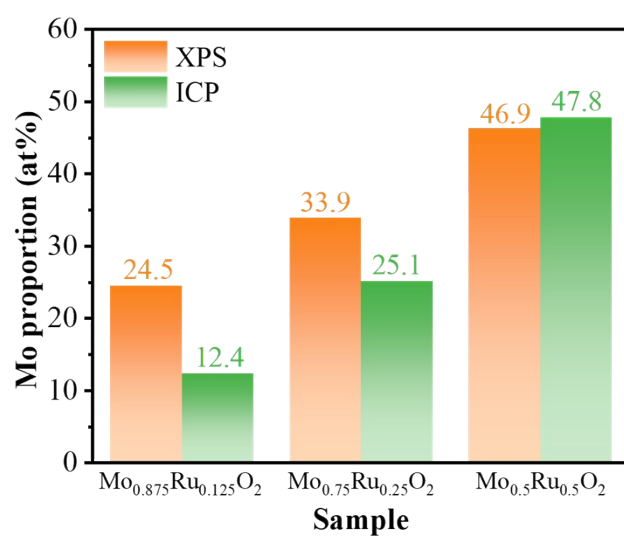
Fig. S14 The Mo proportion obtained by XPS and ICP.

RuO$_2$ slab

Mo$_2$Ru$_{14}$O$_{32}$ slab

Mo$_4$Ru$_{12}$O$_{32}$ slab

Mo$_8$Ru$_8$O$_{32}$ slab

Mo$_2$Ru$_{14}$O$_{32\text{-Osat}}$ slab

Mo$_4$Ru$_{12}$O$_{32\text{-Osat}}$ slab

Mo$_8$Ru$_8$O$_{32\text{-Osat}}$ slab
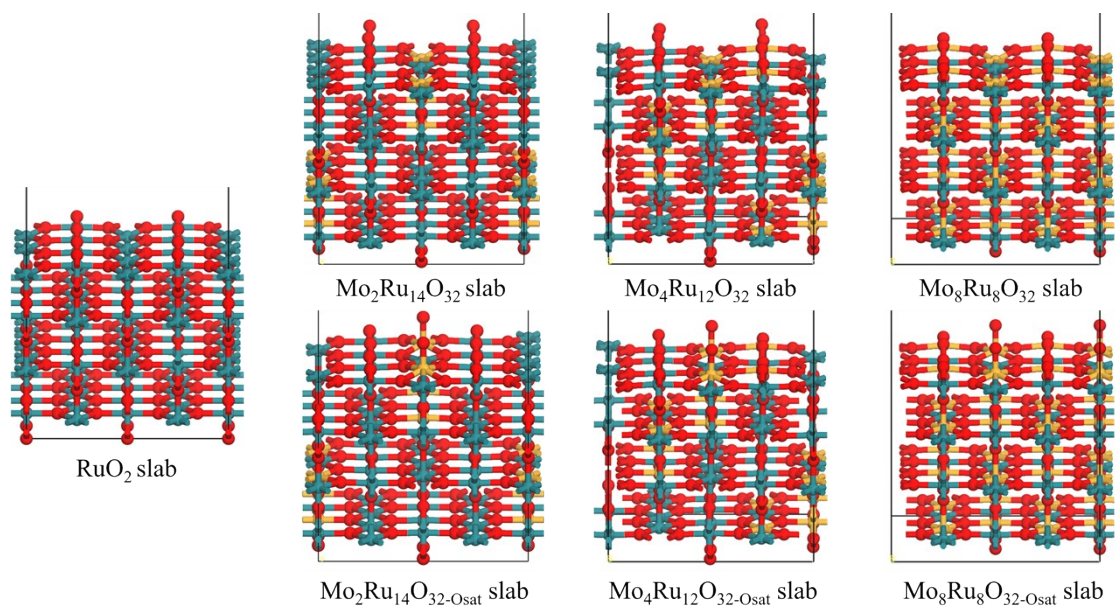
Fig. S15 Initial and oxygen-saturated slab models with different Mo proportion.
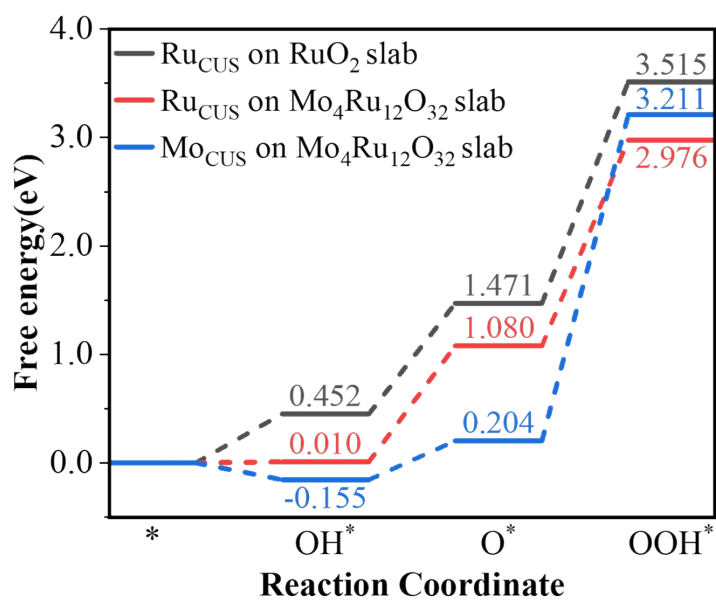
Fig. S16 Free energy diagram of surface hydroxylation on CUSs of the RuO_2 and $Mo_4Ru_{12}O_{32}$ slabs.
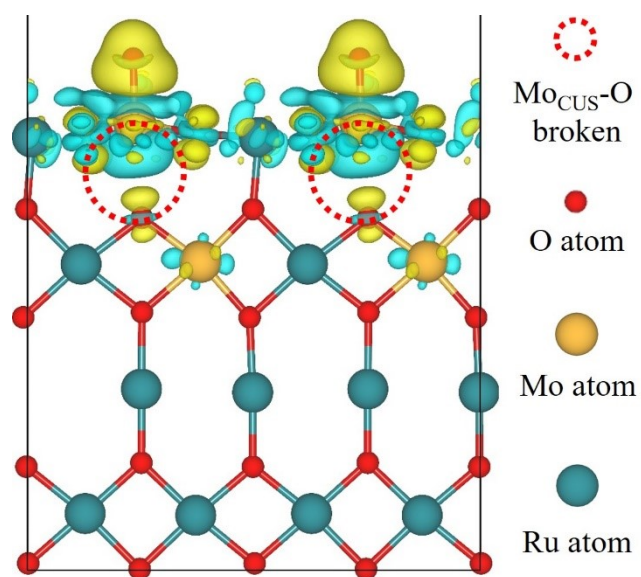
Fig. S17 Differential charge density diagram after surface hydroxylation on Mo_{CUS}.
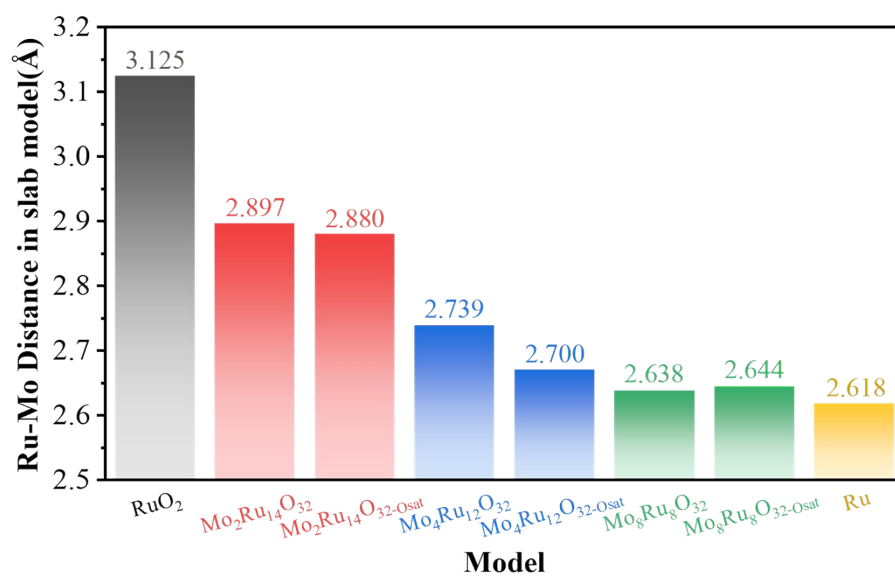
Fig. S18 Ru-Ru/Mo coordination distance on RuO_2, $Mo_xRu_{16-x}O_{32}$, metal Ru slabs before and after the formation of O^*.
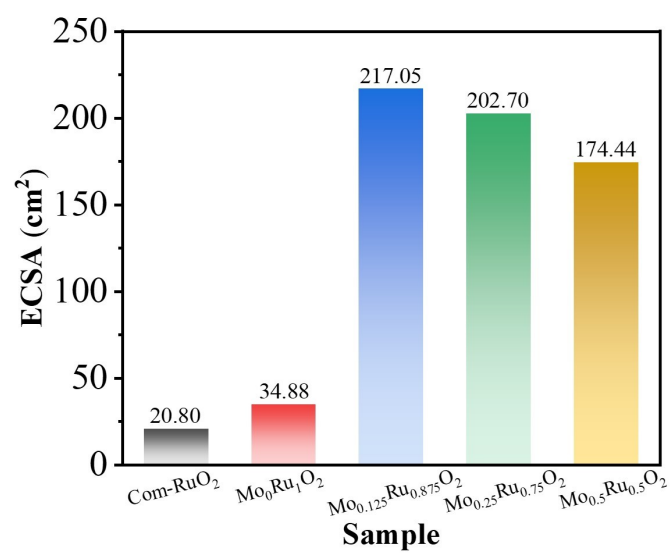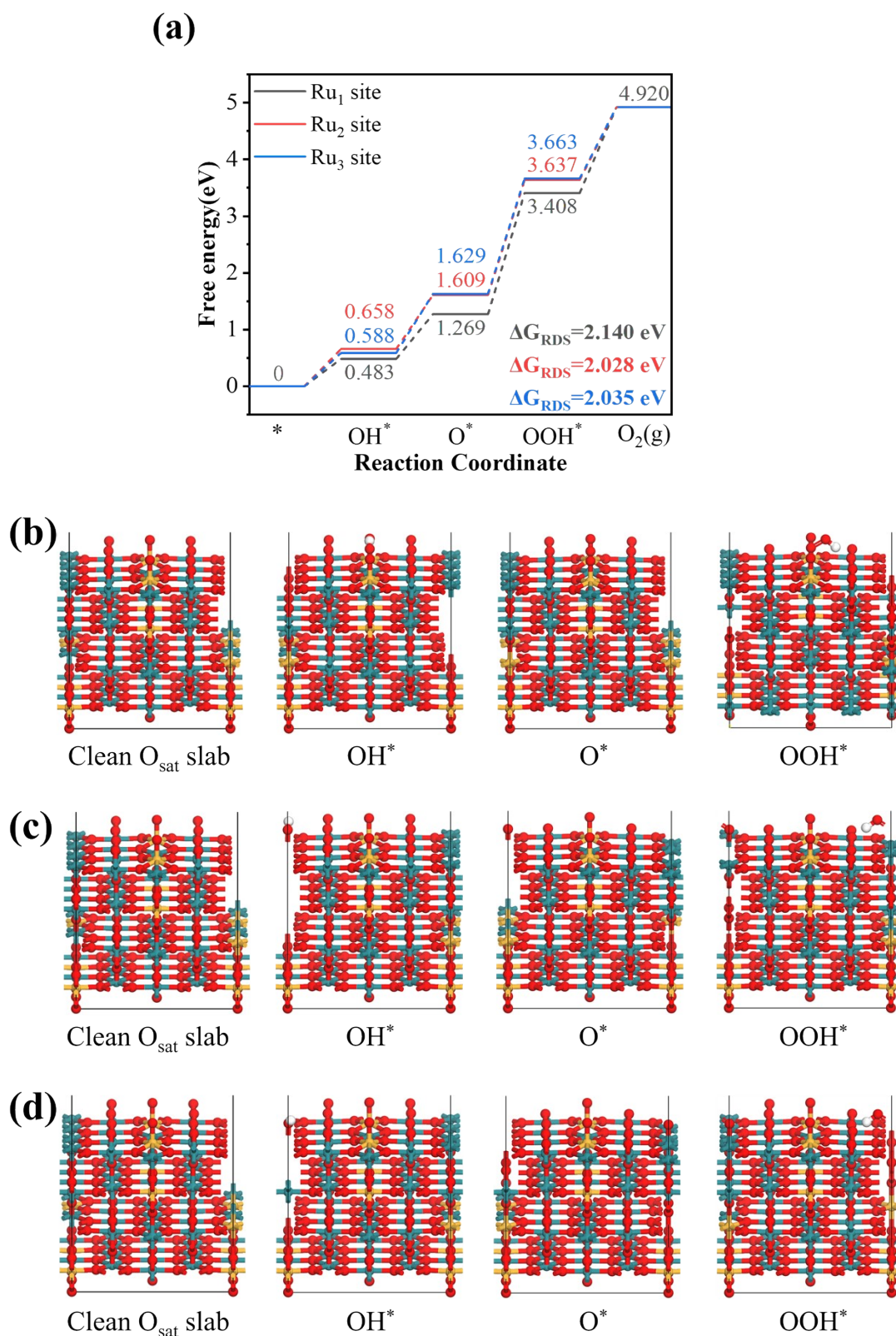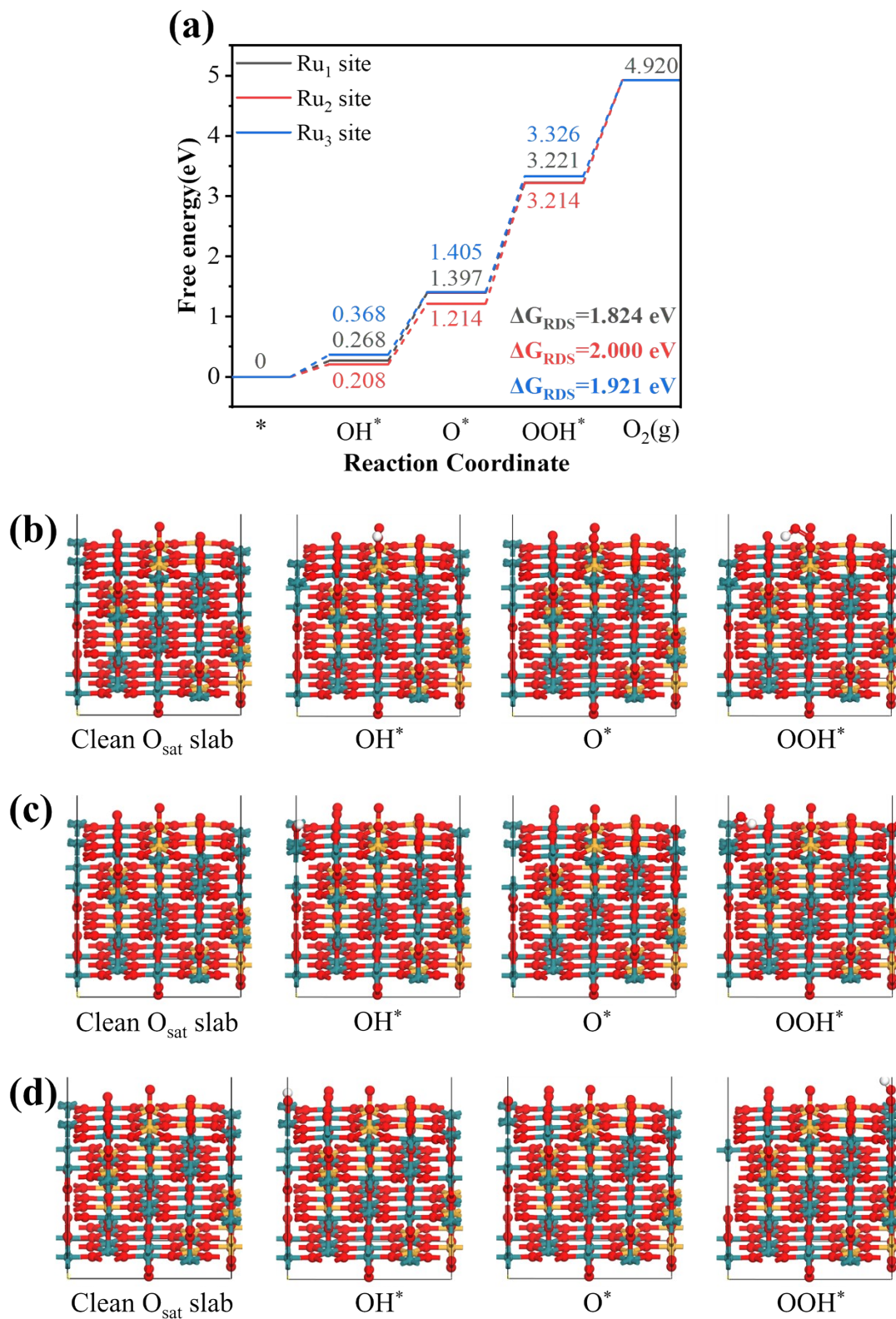
Fig. S19 ECSA of Com-RuO$_2$ and Mo-doped RuO$_2$.

(a)

(b)

Clean slab   OH*   O*   OOH*
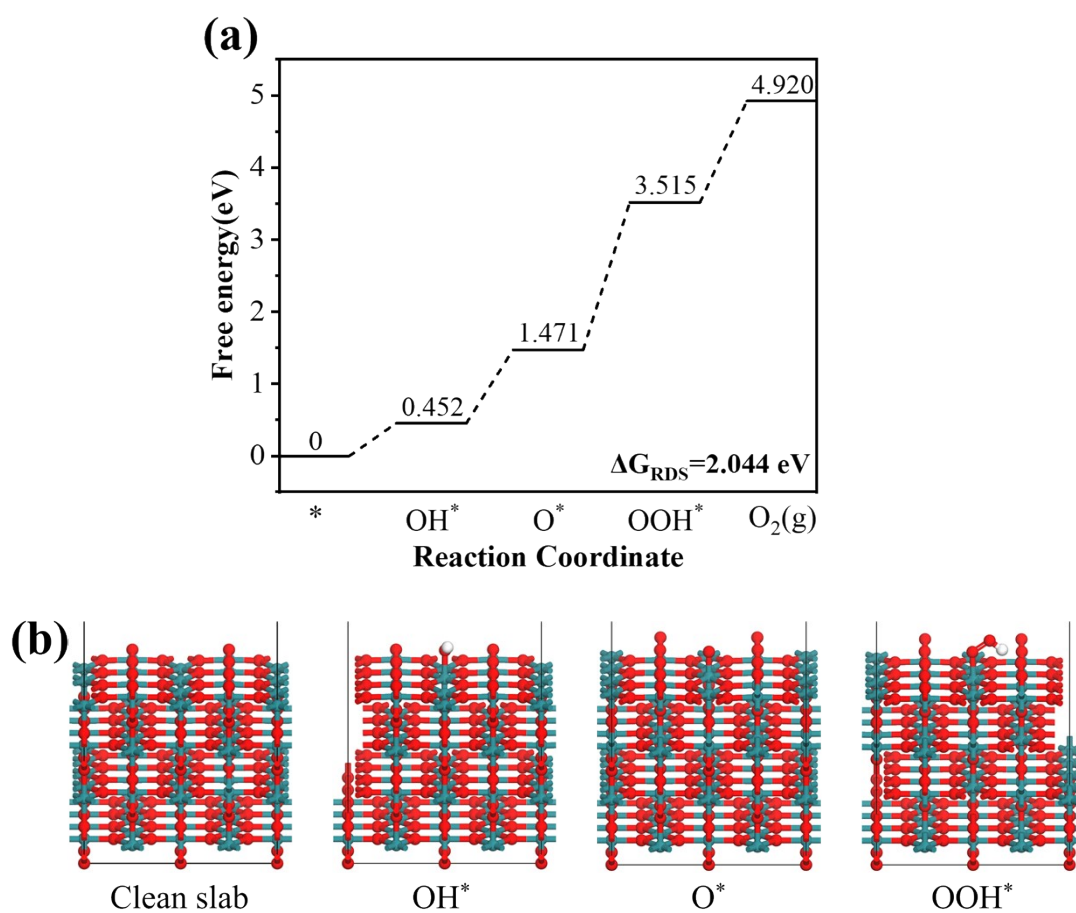
Fig. S20 a) Free energy step diagram and **b)** corresponding structures of RuO_2.

(a)

(b)

Clean O$_{sat}$ slab   OH*   O*   OOH*

(c)

Clean O$_{sat}$ slab   OH*   O*   OOH*

(d)

Clean O$_{sat}$ slab   OH*   O*   OOH*

Fig. S21 a) Free energy step diagram and **b-d)** corresponding structures of Mo$_2$Ru$_{14}$O$_{32\text{-}Osat}$.

Fig. S22 a) Free energy step diagram and **b-d)** corresponding structures of $Mo_4Ru_{12}O_{32-Osat}$.

(a)

(b)

Clean O_{sat} slab OH^* O^* OOH^*
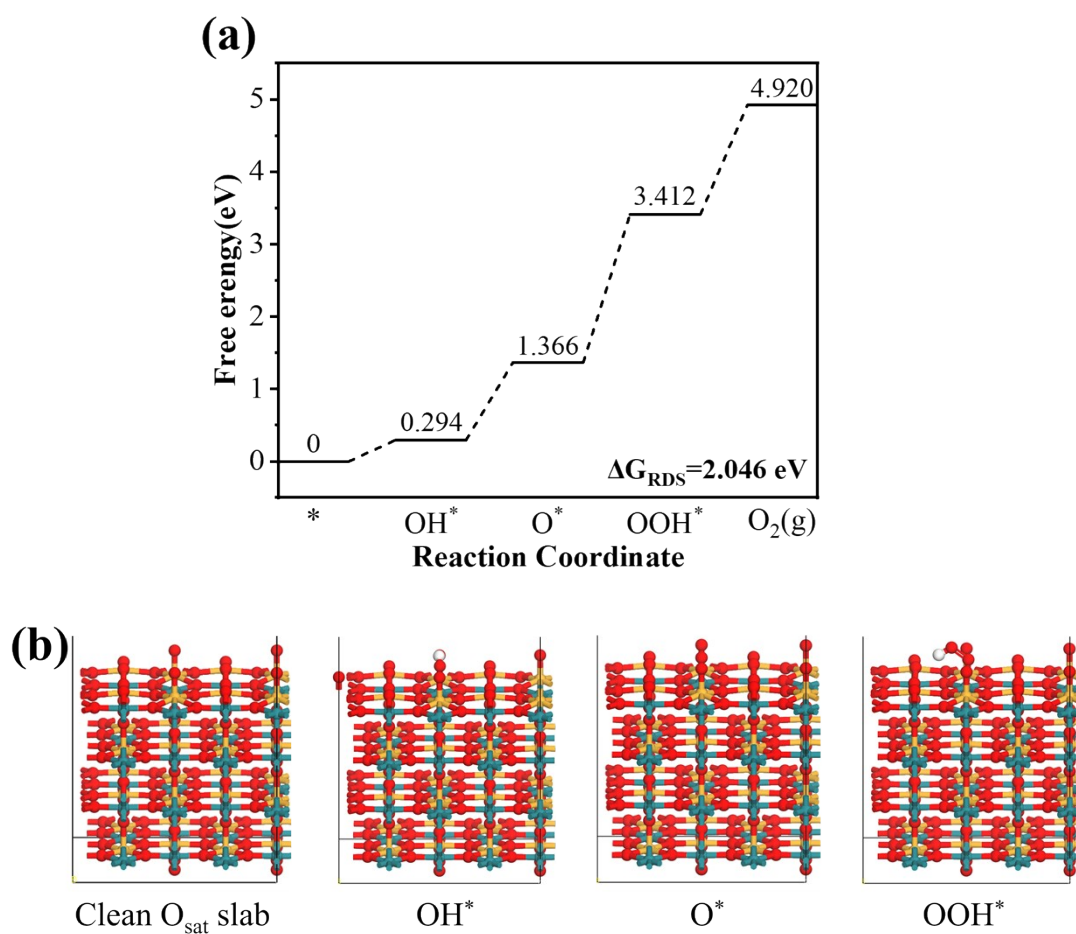
Fig. S23 a) Free energy step diagram and **b)** corresponding structures of $Mo_8Ru_8O_{32\text{-}Osat}$.
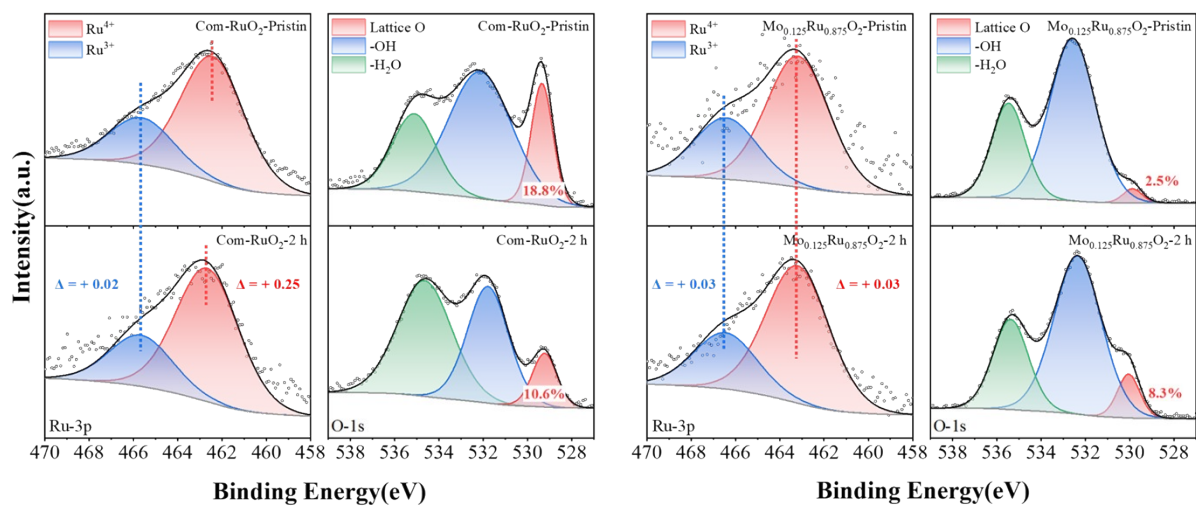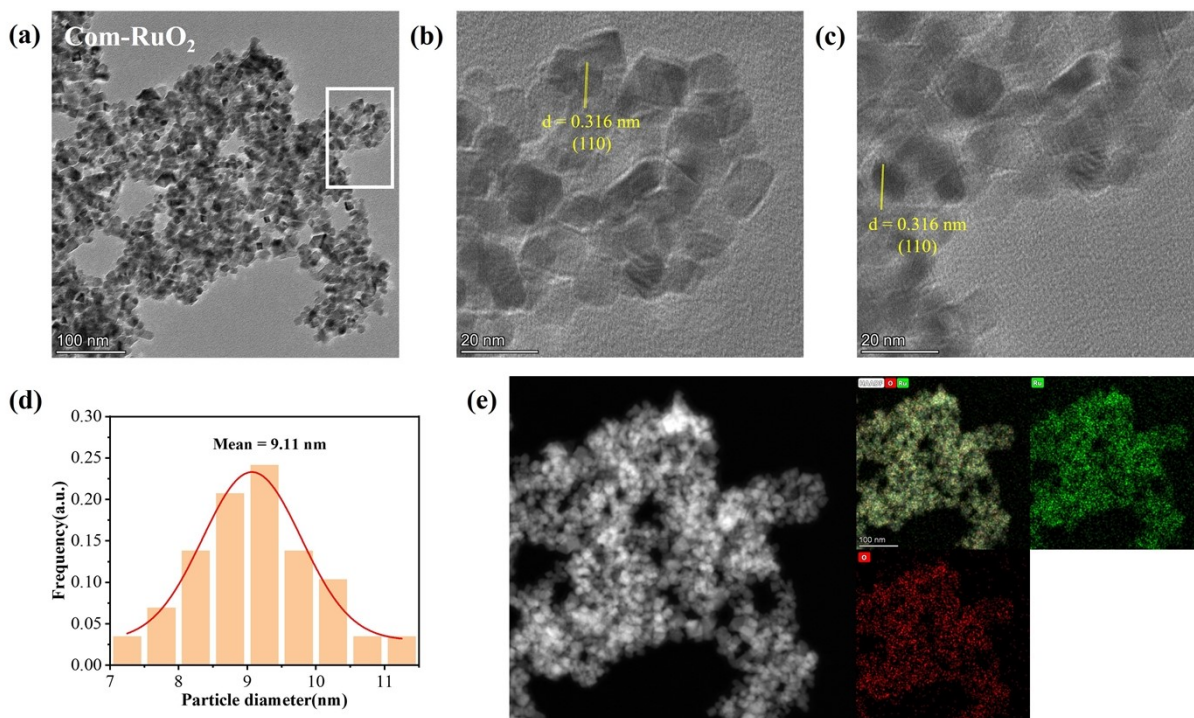
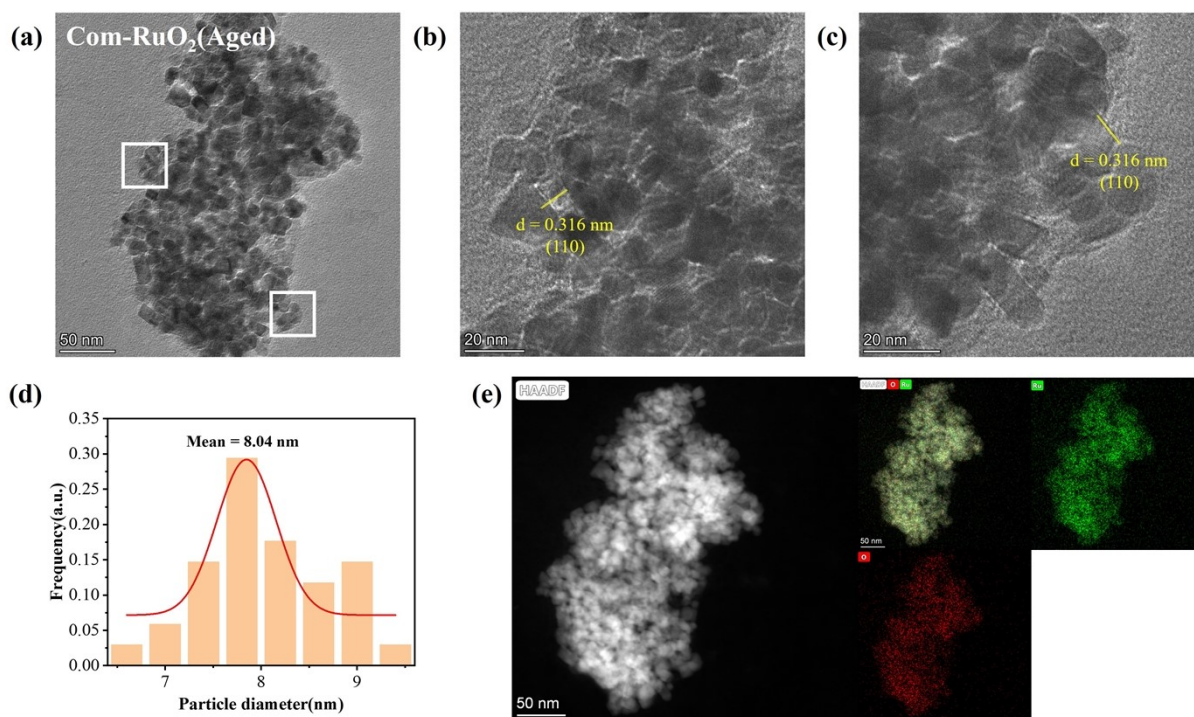**Fig. S24** a) XPS spectra of Com-RuO$_2$ and Mo$_{0.125}$Ru$_{0.875}$O$_2$ after aging for 2 hours.
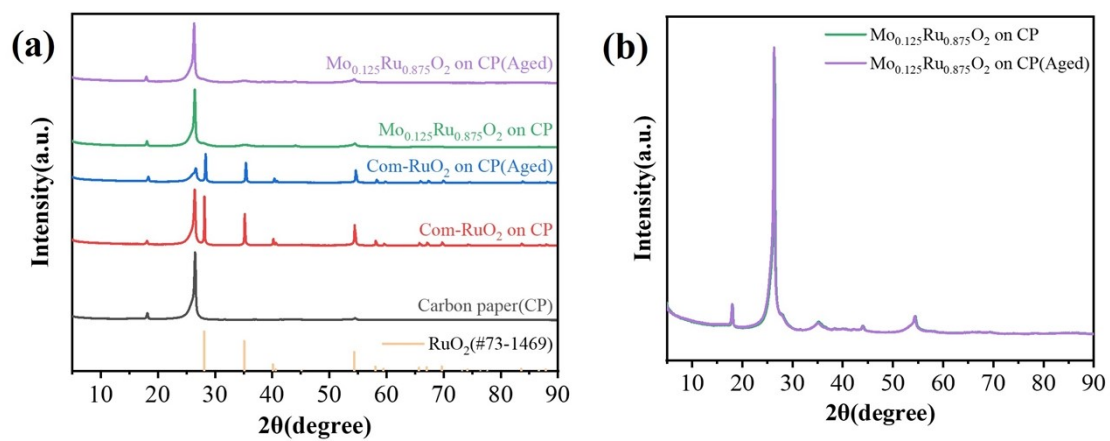
Fig. S25 a) XRD spectra of Com-RuO$_2$ and Mo$_{0.125}$Ru$_{0.875}$O$_2$ before and after aging for 12 hours.
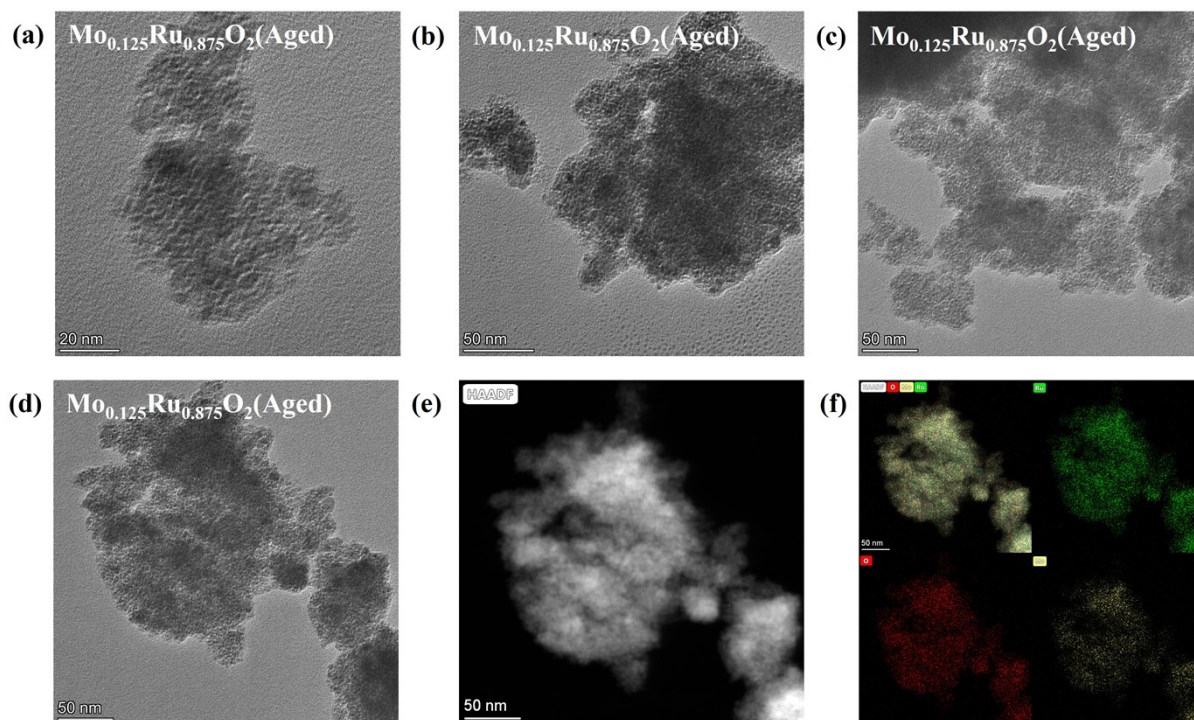
Fig. S26 a-c) TEM images, d) particle size distribution and e) HADDF image and EDS mapping of Com-RuO$_2$ before aging.
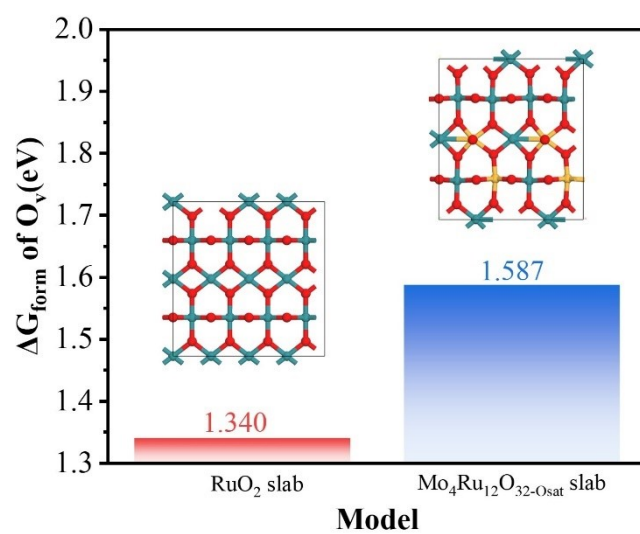
Fig. S27 a-c) TEM images, d) particle size distribution and e) HADDF image and EDS mapping of Com-RuO$_2$ after aging for 12 hours.

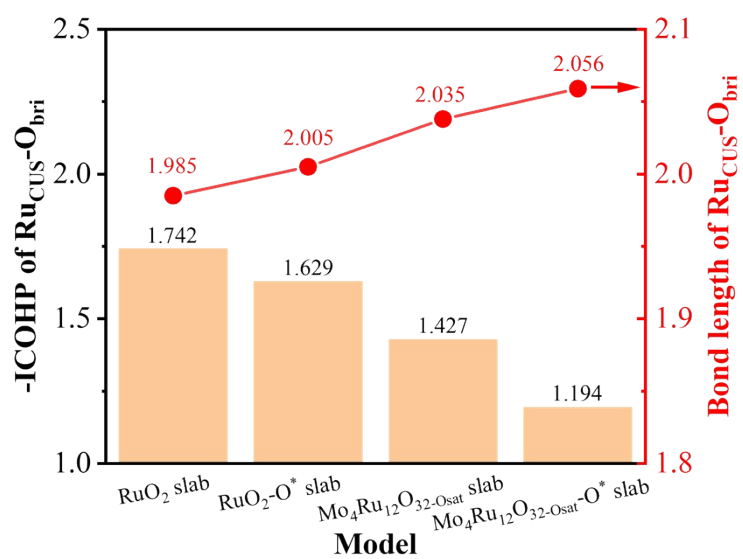**Fig. S28** a-d) TEM images, e) HAADF image and f) EDS mapping of $Mo_{0.125}Ru_{0.875}O_2$ after aging for 12 hours.
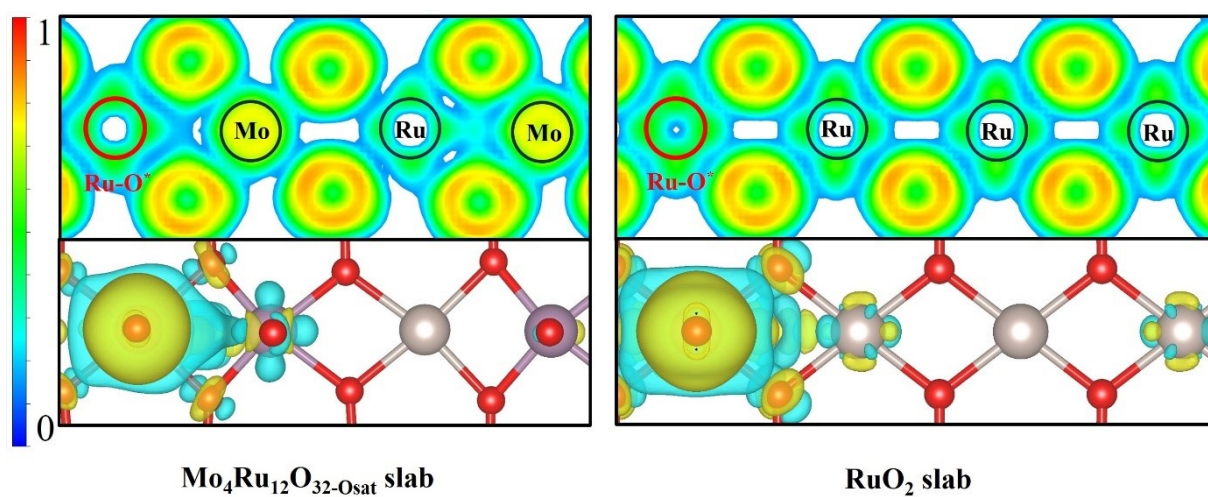
Fig. S29 Formation energy of oxygen vacancies on the RuO_2 slab and $Mo_4Ru_{12}O_{32\text{-}Osat}$ slab.

Fig. S30 -ICOHP and bond length of Ru_{CUS}-O_{bri} bond before and after the formation of O^*.

Fig. S31 ELF after the formation of Ru–O* on the RuO_2 slab and $Mo_4Ru_{12}O_{32}$-$_{Osat}$ slab.

Table S1. Elemental composition analysis of $Mo_xRu_{1-x}O_2$ by ICP-AES.

ICP results			
Sample	Element	Mass fraction	Atomic fraction
$Mo_{0.125}Ru_{0.875}O_2$	Mo	3.8330%	12.4%
	Ru	28.4941%	87.6%
$Mo_{0.25}Ru_{0.75}O_2$	Mo	8.1784%	25.1%
	Ru	25.6610%	74.8%
$Mo_{0.5}Ru_{0.5}O_2$	Mo	16.2548%	47.8%
	Ru	18.7269%	52.2%

Table S2. Bader charge of Ru and/or Mo in bulk of RuO_2, $Mo_xRu_{16-x}O_{32}$, MoO_2 and MoO_3.

Model	Bader charge of Ru atom	Bader charge of Mo atom
$RuO_{2\text{-bulk}}$	1.723	/
$Mo_2Ru_{14}O_{32\text{-bulk}}$	1.686	2.434
$Mo_4Ru_{12}O_{32\text{-bulk}}$	1.650	2.415
$Mo_8Ru_8O_{32\text{-bulk}}$	1.523	2.364
$MoO_{2\text{-bulk}}$ ($P2_1/c$)	/	2.107
$MoO_{3\text{-bulk}}$	/	2.639

Table S3. EXAFS data fitting results of Ru-foil, $Mo_{0.125}Ru_{0.875}O_2$ and RuO_2 ($S_0^2 = 0.8$).

Sample	Path	CN^a	$R(Å)^b$	$\sigma^2(Å^2)^c$	$\Delta E_0(eV)^d$	R-factor
Ru-foil	Ru-Ru$_1$	6	2.652±0.002	0.00806	2.762	0.0217
	Ru-Ru$_2$	6	2.675±0.021	0.00210		
$Mo_{0.125}Ru_{0.875}O_2$	Ru-O	4.41±1.58	2.064±0.003	0.00855	-0.363	0.0327
	Ru-Mo	0.74±0.26	2.726±0.016	0.00897		
Com-RuO$_2$	Ru-O	6	1.969±0.025	0.00172	-2.684	0.0179
	Ru-Ru$_1$	2	3.138±0.014	0.00199		
	Ru-Ru$_2$	8	3.561±0.003	0.00221		

[a] coordination number, [b] coordination distance, [c] Debye-waller factor, [d] inner potential shift

Table S4. EIS fitting parameters for all samples.

Sample	R_s (ohm)	R_{ct} (ohm)	CPE-T	CPE-P
Com-RuO$_2$	27.14	8189	0.002425	0.93673
Mo$_0$Ru$_1$O$_2$	29.67	1144	0.003229	0.92418
Mo$_{0.125}$Ru$_{0.875}$O$_2$	25.11	462	0.010153	0.88435
Mo$_{0.25}$Ru$_{0.75}$O$_2$	26.24	778	0.010241	0.86744
Mo$_{0.5}$Ru$_{0.5}$O$_2$	28.57	1098	0.008857	0.81717

Table S5. Catalogue of reaction interfaces for $Mo_xRu_{1-x}O_2$.

Sample	Mo at% from ICP	Corresponding Bulk model	Mo at% from XPS	Corresponding Slab model
Com-RuO$_2$	0.0 at%	RuO$_{2\text{-bulk}}$	0.0 at%	RuO$_2$
Mo$_{0.125}$Ru$_{0.875}$O$_2$	12.4 at%	Mo$_2$Ru$_{14}$O$_{32\text{-bulk}}$	24.5 at%	Mo$_4$Ru$_{12}$O$_{32}$-O$_{sat}$
Mo$_{0.25}$Ru$_{0.75}$O$_2$	25.1 at%	Mo$_4$Ru$_{12}$O$_{32\text{-bulk}}$	33.9 at%	/
Mo$_{0.5}$Ru$_{0.5}$O$_2$	47.8 at%	Mo$_8$Ru$_8$O$_{32\text{-bulk}}$	46.3 at%	Mo$_8$Ru$_8$O$_{32}$-O$_{sat}$

Table S6. Comparison of the OER performance of reported representative Ru-based oxide electrocatalysts in acidic media.

Catalyst	Overpotential (mV@10 mA cm^{-2})	Stability(h) @10 mA cm^{-2}	Stability in PEMWE (h)	Reference
$Mo_{0.125}Ru_{0.875}O_2$	224	>400	500 h@300 mA cm^{-2}	This work
$Li_{0.52}RuO_2$	152	70	/	[4]
a/c-RuO_2(Na-doped)	205	60	/	[8]
$Cr_{0.6}Ru_{0.4}O_2$	178	10	/	[9]
$Mn_{0.4}Ru_{0.6}O_2$	196	120	12 h@1 A cm^{-2}	[10]
$RuCoO_x$	200	100	10 h@100 mA cm^{-2}	[11]
Ni-RuO_2	214	200	1000 h@200 mA cm^{-2}	[12]
Cu-RuO_2	188	8	/	[13]
$ZnRuO_x$	230	320	120 h@200 mA cm^{-2}	[14]
Ga-RuO_2	218	150		[15]
$Nb_{0.1}Ru_{0.9}O_2$	204	360	100 h@200 mA cm^{-2}	[16]
In-RuO_2/G	187	180	/	[17]
Er-RuO_x	200	200	100 h@200 mA cm^{-2}	[7]
Ta-RuO_2	201	280	/	[18]
Ru_5WO_x	227	550	/	[19]

Supplementary References

(1) Kresse, G.; Furthmuller, J. Efficiency of ab-initio total energy calculations for metals and semiconductors using a plane-wave basis set. *Computational Materials Science* **1996**, *6*, 15-50.

(2) Kresse, G.; Furthmuller, J. Efficient iterative schemes for ab initio total-energy calculations using a plane-wave basis set. *Phys Rev B* **1996**, *54*, 11169-11186.

(3) Kresse, G.; Hafner, J. Ab initio molecular dynamics for liquid metals. *Phys Rev B Condens Matter* **1993**, *47* (1), 558-561.

(4) Qin, Y.; Yu, T.; Deng, S.; Zhou, X. Y.; Lin, D.; Zhang, Q.; Jin, Z.; Zhang, D.; He, Y. B.; Qiu, H. J.; et al. RuO(2) electronic structure and lattice strain dual engineering for enhanced acidic oxygen evolution reaction performance. *Nat Commun* **2022**, *13* (1), 3784.

(5) Hao, S.; Liu, M.; Pan, J.; Liu, X.; Tan, X.; Xu, N.; He, Y.; Lei, L.; Zhang, X. Dopants fixation of Ruthenium for boosting acidic oxygen evolution stability and activity. *Nat Commun* **2020**, *11* (1), 5368.

(6) Du, K.; Zhang, L.; Shan, J.; Guo, J.; Mao, J.; Yang, C. C.; Wang, C. H.; Hu, Z.; Ling, T. Interface engineering breaks both stability and activity limits of RuO(2) for sustainable water oxidation. *Nat Commun* **2022**, *13* (1), 5448.

(7) Li, L.; Zhang, G.; Zhou, C.; Lv, F.; Tan, Y.; Han, Y.; Luo, H.; Wang, D.; Liu, Y.; Shang, C.; et al. Lanthanide-regulating Ru-O covalency optimizes acidic oxygen evolution electrocatalysis. *Nat Commun* **2024**, *15* (1), 4974.

(8) Zhang, L.; Jang, H.; Liu, H.; Kim, M. G.; Yang, D.; Liu, S.; Liu, X.; Cho, J. Sodium-Decorated Amorphous/Crystalline RuO(2) with Rich Oxygen Vacancies: A Robust pH-Universal Oxygen Evolution Electrocatalyst. *Angew Chem Int Ed Engl* **2021**, *60* (34), 18821-18829.

(9) Lin, Y.; Tian, Z.; Zhang, L.; Ma, J.; Jiang, Z.; Deibert, B. J.; Ge, R.; Chen, L. Chromium-ruthenium oxide solid solution electrocatalyst for highly efficient oxygen evolution reaction in acidic media. *Nat Commun* **2019**, *10* (1), 162.

(10) Tan, L.; Wu, X.; Wang, H.; Zeng, J.; Mei, B.; Pan, X.; Hu, W.; Faiza, M.; Xiao, Q.; Zhao, Y.; et al. Ferromagnetic-Interaction-Induced Spin Symmetry Broken in Ruthenium Oxide for Enhanced Acidic Water Oxidation. *ACS Catalysis* **2024**, *14* (15), 11273-11285.

(11) Zhu, W.; Yao, F.; Cheng, K.; Zhao, M.; Yang, C. J.; Dong, C. L.; Hong, Q.; Jiang, Q.; Wang, Z.; Liang, H. Direct Dioxygen Radical Coupling Driven by Octahedral Ruthenium-Oxygen-Cobalt Collaborative Coordination for Acidic Oxygen Evolution Reaction. *J Am Chem Soc* **2023**, *145* (32), 17995-18006.

(12) Wu, Z. Y.; Chen, F. Y.; Li, B.; Yu, S. W.; Finfrock, Y. Z.; Meira, D. M.; Yan, Q. Q.; Zhu, P.; Chen, M. X.; Song, T. W.; et al. Non-iridium-based electrocatalyst for durable acidic oxygen evolution reaction in proton exchange membrane water electrolysis. *Nat Mater* **2023**, *22* (1), 100-108.

(13) Su, J.; Ge, R.; Jiang, K.; Dong, Y.; Hao, F.; Tian, Z.; Chen, G.; Chen, L. Assembling Ultrasmall Copper-Doped Ruthenium Oxide Nanocrystals into Hollow Porous Polyhedra: Highly Robust Electrocatalysts for Oxygen Evolution in Acidic Media. *Adv Mater* **2018**, e1801351.

(14) Sun, P.; Qiao, Z.; Dong, X.; Jiang, R.; Hu, Z. T.; Yun, J.; Cao, D. Designing 3d Transition Metal Cation-Doped MRuO(x) As Durable Acidic Oxygen Evolution Electrocatalysts for PEM Water Electrolyzers. *J Am Chem Soc* **2024**, *146* (22), 15515-15524.

(15) Wu, L.; Huang, W.; Li, D.; Jia, H.; Zhao, B.; Zhu, J.; Zhou, H.; Luo, W. Unveiling the Structure and Dissociation of Interfacial Water on RuO(2) for Efficient Acidic Oxygen Evolution Reaction. *Angew Chem Int Ed Engl* **2025**, *64* (1), e202413334.

(16) Liu, H.; Zhang, Z.; Fang, J.; Li, M.; Sendeku, M. G.; Wang, X.; Wu, H.; Li, Y.; Ge, J.; Zhuang, Z.; et al. Eliminating over-oxidation of ruthenium oxides by niobium for highly stable electrocatalytic oxygen evolution in acidic media. *Joule* **2023**, *7* (3), 558-573.

(17) Wang, Y.; Lei, X.; Zhang, B.; Bai, B.; Das, P.; Azam, T.; Xiao, J.; Wu, Z. S. Breaking the Ru-O-Ru Symmetry of a RuO(2) Catalyst for Sustainable Acidic Water Oxidation. *Angew Chem Int Ed Engl* **2024**, *63* (3), e202316903.

(18) Wang, X.; Li, Z.; Jang, H.; Chen, C.; Liu, S.; Wang, L.; Kim, M. G.; Cho, J.; Qin, Q.; Liu, X. RuO2 with Short-Range Ordered Tantalum Single Atoms for Enhanced Acidic Oxygen Evolution Reaction. *Advanced Energy Materials* **2024**.

(19) Wen, Y.; Liu, C.; Huang, R.; Zhang, H.; Li, X.; Garcia de Arquer, F. P.; Liu, Z.; Li, Y.; Zhang, B. Introducing Bronsted acid sites to accelerate the bridging-oxygen-assisted deprotonation in acidic water oxidation. *Nat Commun* **2022**, *13* (1), 4871.